Ballistic InSb nanowires and networks via metal-sown selective area growth

Journal:	*Nano Letters*
Manuscript ID	nl-2019-04265p
Manuscript Type:	Communication
Date Submitted by the Author:	15-Oct-2019
Complete List of Authors:	Aseev, Pavel; Microsoft Quantum Lab Delft Wang, Guanzhong; TU Delft Binci, Luca; TU Delft Singh, Amrita; Microsoft Quantum Lab Delft Martí-Sánchez, Sara; Catalan Institute of Nanoscience and Nanotechnology Botifoll, Marc; Catalan Institute of Nanoscience and Nanotechnology Stek, Lieuwe; Microsoft Quantum Lab Delft Bordin, Alberto; TU Delft Watson, John; Microsoft Quantum Lab Delft Boekhout, Frenk; TNO Abel, Daniel; Microsoft Quantum Lab Delft Gamble, John; Microsoft Corp Van Hoogdalem, Kevin; Microsoft Quantum Lab Delft Arbiol, Jordi; ICREA and Catalan Institute of Nanoscience and Nanotechnology (ICN2), CSIC and The Barcelona Institute of Science and Technology (BIST), Advanced Electron Nanoscopy Kouwenhoven, Leo; Microsoft Quantum Lab Delft de Lange, Gijs; Microsoft Quantum Lab Delft Caroff, Philippe; Microsoft Quantum Lab Delft

Ballistic InSb nanowires and networks via metal-sown selective area growth

Pavel Aseev[1,,†], Guanzhong Wang[2,†], Luca Binci[2,†], Amrita Singh[2], Sara Martí-Sánchez[3], Marc Botifoll[3], Lieuwe J. Stek[2], Alberto Bordin[2], John D. Watson[1], Frenk Boekhout[1,4], Daniel Abel[1], John Gamble[5], Kevin Van Hoogdalem[1], Jordi Arbiol[3,6], Leo P. Kouwenhoven[1,2], Gijs de Lange[1], Philippe Caroff[1,*]*

[1] Microsoft Quantum Lab Delft, Lorentzweg 1, 2628 CJ Delft, Netherlands.

[2] QuTech and Kavli Institute of NanoScience, Delft University of Technology, Lorentzweg 1, 2600 GA Delft, The Netherlands.

[3] Catalan Institute of Nanoscience and Nanotechnology (ICN2), CSIC and BIST, Campus UAB, 08193 Bellaterra, Barcelona, Catalonia, Spain

[4] QuTech and Netherlands Organization for Applied Scientific Research (TNO), Stieltjesweg 1, 2628 CK Delft, The Netherlands

[5] Microsoft Quantum, 1 Redmond Way, Redmond, WA 98052 USA

[6] ICREA, Pg. Lluí s Companys 23, 08010 Barcelona, Catalonia, Spain

KEYWORDS: InSb, molecular beam epitaxy, selective area growth, droplet epitaxy.

Table of content graphic:

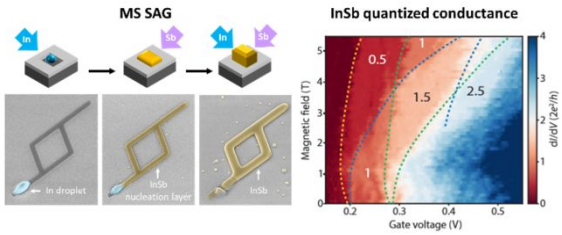

ABSTRACT

Selective area growth is a promising technique to realize semiconductor-superconductor hybrid nanowire networks potentially hosting topologically protected Majorana-based qubits. In some cases, however, such as molecular beam epitaxy of InSb on InP or GaAs substrates, nucleation and selective growth conditions do not necessarily overlap. To overcome this challenge we propose Metal-Sown Selective Area Growth (MS SAG) technique which allows decoupling selective deposition and nucleation growth conditions by temporarily isolating these stages. It consists of three steps: (i) selective deposition of In droplets only inside the mask openings at relatively high temperatures favoring selectivity, (ii) nucleation of InSb under Sb flux from In droplets which act as a reservoir of group III adatoms, done at relatively low temperatures favoring nucleation of InSb, (iii) homoepitaxy of InSb on top of formed nucleation

layer under simultaneous supply of In and Sb fluxes at conditions favoring selectivity and high crystal quality. We demonstrate that complex InSb nanowire networks of high crystal and electrical quality can be achieved this way. We extract mobility values of 10,000–25,000 $cm^2\ V^{-1}\ s^{-1}$ consistently from field-effect and Hall mobility measurements across single nanowire segments as well as wires with junctions. Moreover, we demonstrate ballistic transport in a 440 nm long channel in a single nanowire under magnetic field below 1 T. We also extract a phase-coherent length of ~8 μm at 50 mK in mesoscopic rings.

Semiconductor-superconductor hybrid nanowire (NW) networks are promising candidates for hosting topologically protected Majorana-based qubits, which have a potential to revolutionize the emerging field of quantum computing.[1] The III-V semiconductor InSb is of particular interest in this regard owing to its large *g*-factor, which enables a relatively small magnetic field to drive a hybrid semiconductor-superconductor NW into the topological regime. Moreover the small effective mass favorably leads to a large subband spacing.[2] So far, mostly single[3] or small-scale networks[4] of InSb NWs were used in Majorana-related transport experiments. To support further progress in the field,

advanced NW networks are needed to fulfill the requirements of recent theoretical proposals.[5–8] Selective area growth (SAG) is a promising technique for realization of in-plane NW networks, where a crystalline III-V substrate is covered with an amorphous mask and growth proceeds selectively only inside lithographically defined openings. However, early results suggest that in contrast to well-studied III-V materials such as InAs and GaAs,[9–11] the special case of InSb SAG by molecular beam epitaxy (MBE) has selectivity conditions that do not overlap with its preferred nucleation conditions.[12,13] This can be overcome by using hydrogen plasma during the growth of InSb but at the cost of reduced shape uniformity of different NWs and networks.[12,13]

In this work we implement a Metal-Sown Selective Area Growth (MS SAG) technique which allows to decouple nucleation and selective growth conditions. MS SAG consists of three steps schematically outlined in **Figure 1 a**:

(i) Selective metal sowing – supplying only In flux at relatively high substrate temperature favoring selective In droplets (“seeds”) deposition only inside the mask openings,

(ii) InSb nucleation layer – supplying only Sb flux (”watering”) to convert In droplets into InSb networks at relatively low temperatures which favor nucleation of InSb; In droplets act as a sole source of group-III element in that case.

(iii) Homoepitaxy of InSb on top of the nucleation layer - growth is continued under simultaneous supply of In and Sb fluxes at conditions favoring selectivity and high crystal quality; improving faceting and achieving desired out-of-plane dimensions.

The broad applicability of developed technique is confirmed by successful fabrication of InSb NW networks on InP and GaAs substrates of both <001> and <111>B orientations with InP(111)B case being studied in details. The high crystal quality and composition of both isolated NW segments and junctions are demonstrated by Aberration Corrected High Angle Annular Dark Field Scanning Transmission Electron Microscopy (AC-HAADF-STEM) and Electron Energy Loss Spectroscopy (EELS). Consistent mobility values are extracted from field-effect and Hall mobility measurements across single NW segments

as well as wires with junctions. Moreover, we demonstrate ballistic and phase-coherent transport in single NWs and mesoscopic rings, respectively.

All samples presented in this work are grown by MBE. Prior to loading in the MBE chamber, a hard mask is fabricated by covering the substrate with ~14 nm thick amorphous dielectric layer by plasma-enhanced chemical vapor deposition in which the NW pattern is defined by standard lithography techniques.[9,10] The substrate temperature (T) is measured by a calibrated pyrometer for $T >$ 500 °C and by extrapolating pyrometer values using a thermocouple reading for $T <$ 500 °C. Fluxes of In (F_{In}) and Sb (F_{Sb}) are presented in equivalent planar InSb monolayers per second (ML_{InSb}/s).[9,14] A standard substrate deoxidation procedure is used where it is kept under As flux ($4x10^{-6}$ torr) for 5 min for both GaAs and InP substrates at T = 580 and 500 °C, respectively. Note that 500 °C is the highest temperature used in the entire process of InSb MS SAG on InP substrates which makes it compatible with CMOS technology. In the following text the case of InSb MS SAG on InP(111)B substrate is described in detail, while similar considerations hold for other substrates as demonstrated by successful growth of InSb MS SAG on GaAs(001) (see **Supporting Information SA**).

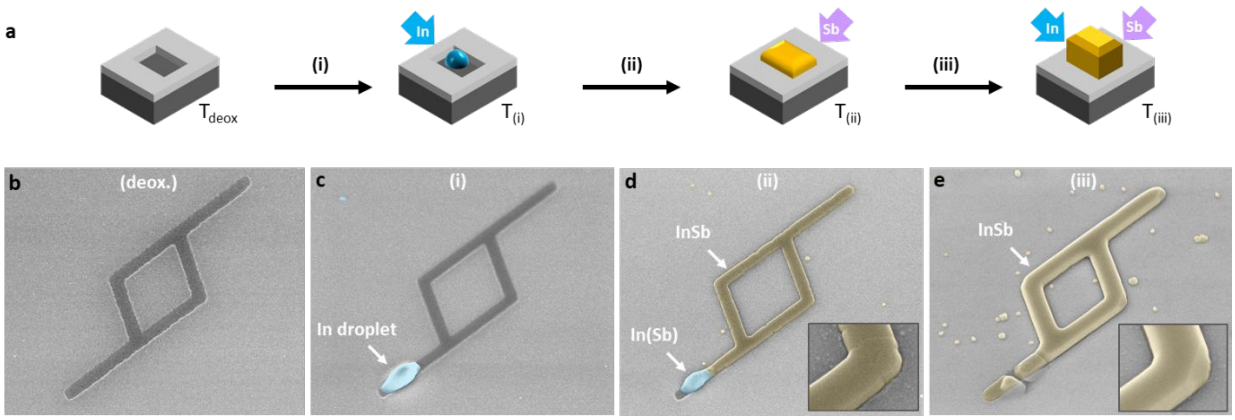

Figure 1. MS SAG of InSb NW networks. **(a)** Schematics of MS SAG step sequence with SEM images (40° tilt) illustrating the individual steps on patterned InP(111)B substrates: **(b)** deoxidized substrate, **(c)** step (i), selective sowing of In at $T_{(i)}$ = 465 °C, **(d)** step (ii), conversion of In into InSb solely under Sb flux at $T_{(ii)}$ = 360 °C, **(e)** step(iii), continuing in conventional SAG regime with simultaneous supply of In and Sb fluxes at $T_{(iii)}$ = 430 °C. Insets highlight faceting evolution from (ii) to (iii).

In a previous work, we demonstrated selective homoepitaxy of InSb wires on InSb(111)B and InSb(001) substrates following conventional SAG method.[9] However, in case of heteroepitaxy of InSb on InP(111)B the conventional SAG method, in which both elemental fluxes provided continuously, results in poor filling of the mask openings due to unfavorable nucleation. This is true for SAG at both the relatively high substrate temperature of T = 430 °C favoring selectivity conditions (**Supporting Information Figure S3 a**)[15] and all the way down to the relatively low substrate temperature of T = 360 °C

favoring nucleation of planar InSb layers (**Supporting Information Figure S3 b**).[16] To overcome this issue, we have turned our attention to an Sb-induced growth technique previously proposed for planar InSb growth for the case when the optimal growth conditions are not known.[14] In that method In is pre-deposited in the absence of Sb flux and then converted into planar InSb via exposure to Sb flux (under no concomitant group III flux).[17] For planar growth on unmasked substrate this process can be monitored by an *in situ* reflection high-energy electron diffraction (RHEED) method.[14] We have observed clear RHEED signal intensity oscillations on planar InSb(001) surfaces, indicating layer-by-layer growth, for substrate temperatures up to T_{crit} = 400 °C, above which no oscillations were visible (**Supporting Information Figure S4**).

In this work we have adapted the above described Sb-induced growth technique to substrates with patterned amorphous masks. Here we give a more detailed description of individual steps during MS SAG (**Figure 1 a**).

After successful deoxidation (**Figure 1 b**), during step (i), only an In flux is supplied to the sample at elevated substrate temperature $T_{(i)}$ resulting in stochastic positioning of In droplets selectively inside the mask openings (see **Figure 1 c**). This becomes possible

due to the higher desorption rate of In adatoms from the amorphous mask compared to crystalline substrate surface.[9] Note that we have observed the mask dielectric layer being occasionally damaged by the droplet (See **Supporting Information SD**).

During step (ii) the substrate temperature is decreased to $T_{(ii)} \leq T_{crit}$ for the subsequent conversion of In into InSb under Sb flux (without concomitant In flux) to form the InSb nucleation layer. Note that despite the fact that only Sb flux is being supplied to the surface the growth proceeds under a local In-rich regime around the droplet because it acts as a metal source. However, this growth mode is not to be confused with standard in-plane vapour-liquid-solid where the droplet is moving along with growth front.[18–21] Resulting InSb NW networks filling the mask openings can be seen in **Figure 1 d**. Attempts to convert In into InSb above T_{crit} result in poor nucleation and highly non-uniform growth, similarly to conventional SAG, as shown in **Supporting Information Figure S3 b**.

During the last step (iii) the substrate temperature is raised to $T_{(iii)}$ at which InSb growth can be continued via a conventional SAG method with both In and Sb fluxes supplied simultaneously. Here the importance of previous steps (i)+(ii) is demonstrated when comparing step (iii) of InSb MS SAG (**Figure 1 d**) to InSb growth without nucleation layer

(**Supporting Information Figure S3 a**), performed under the same growth conditions. Indeed, InSb growth proceeds *uniformly* only in the regions where it is already nucleated and not on bare InP(111)B surfaces. As can be seen in **Figure 1 d** (inset) the InSb NW networks faceting improves at the step (iii), except for the region next to the initial In droplet position, where growth is not uniform. A similar effect was reported for quantum nanorings obtained via droplet epitaxy and is attributed to droplet induced damage of surrounding III-V surface[22]. Because of this limitation, the active region of devices should be carefully selected to be away from the droplet.

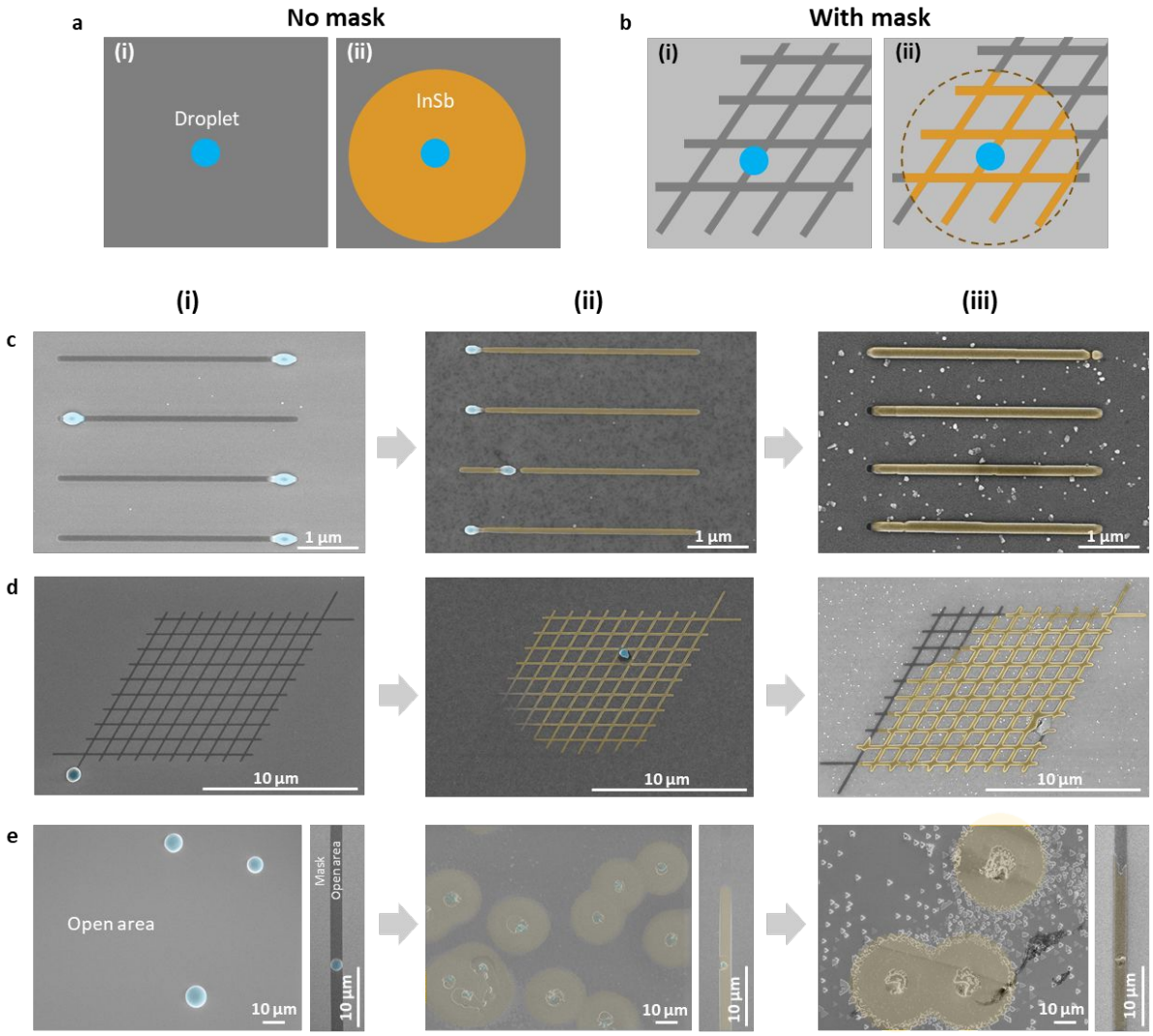

Figure 2. Schematics of diffusion limited growth during the MS SAG for samples **(a)** w/o and **(b)** w/ the mask. SEM images illustrating InSb MS SAG steps for mask openings comprising of **(c)** 100 nm-wide stripes, **(d)** interconnected networks of 130 nm-wide stripes, **(e)** large open areas and 2 µm-wide stripes.

We emphasize that metal droplets formed during MS SAG step (i) act as a sole source of group III adatoms during step (ii). Therefore, the maximum characteristic in-plane size of NW network is defined by surface diffusion length (D) of In adatoms on InP surface at

step (ii) as schematically illustrated in **Figure 2 a, b**. This effect becomes evident when comparing InSb growth evolution during MS SAG in mask openings of different characteristic sizes and geometries (**Figure 2 c, d, e**). Following the methodology proposed for III-V droplet epitaxy[23,24] we have estimated $D_{(ii)}$ = 25,8 ± 1,3 μm at $T_{(ii)}$ = 360 °C from the diameter of the InSb spread around the initial droplet position on large open areas of InP surface (**Figure 2 e**). Note that in case of complex networks D can be significantly reduced due to non-trivial migration paths introduced by mask confinement (see **Figure 2 d** panel (ii)).

Previously it was demonstrated that D can be improved by increasing the substrate temperature and/or decreasing group V flux.[23,24] However, there is limit to such improvement due to T_{crit} and the finite diffusion length of In adatoms under vacuum conditions, which we determined to be $D_{(i)}$ = 52 ± 14 μm (at T = 465 °C and residual pressure in the chamber of $1x10^{-10}$ torr). Future work is required to overcome this limit.

Direct measurements of $D_{(iii)}$ are complicated due to InSb lateral growth being suppressed by non-favorable nucleation conditions in the mask regions which are not already filled with InSb (e.g. **Figure 2 d** panels (ii) and (iii)). However, it is reasonable to

assume that $D_{(iii)} \geq D_{(ii)}$ because of homogeneous out-of-plane growth of the InSb segments.

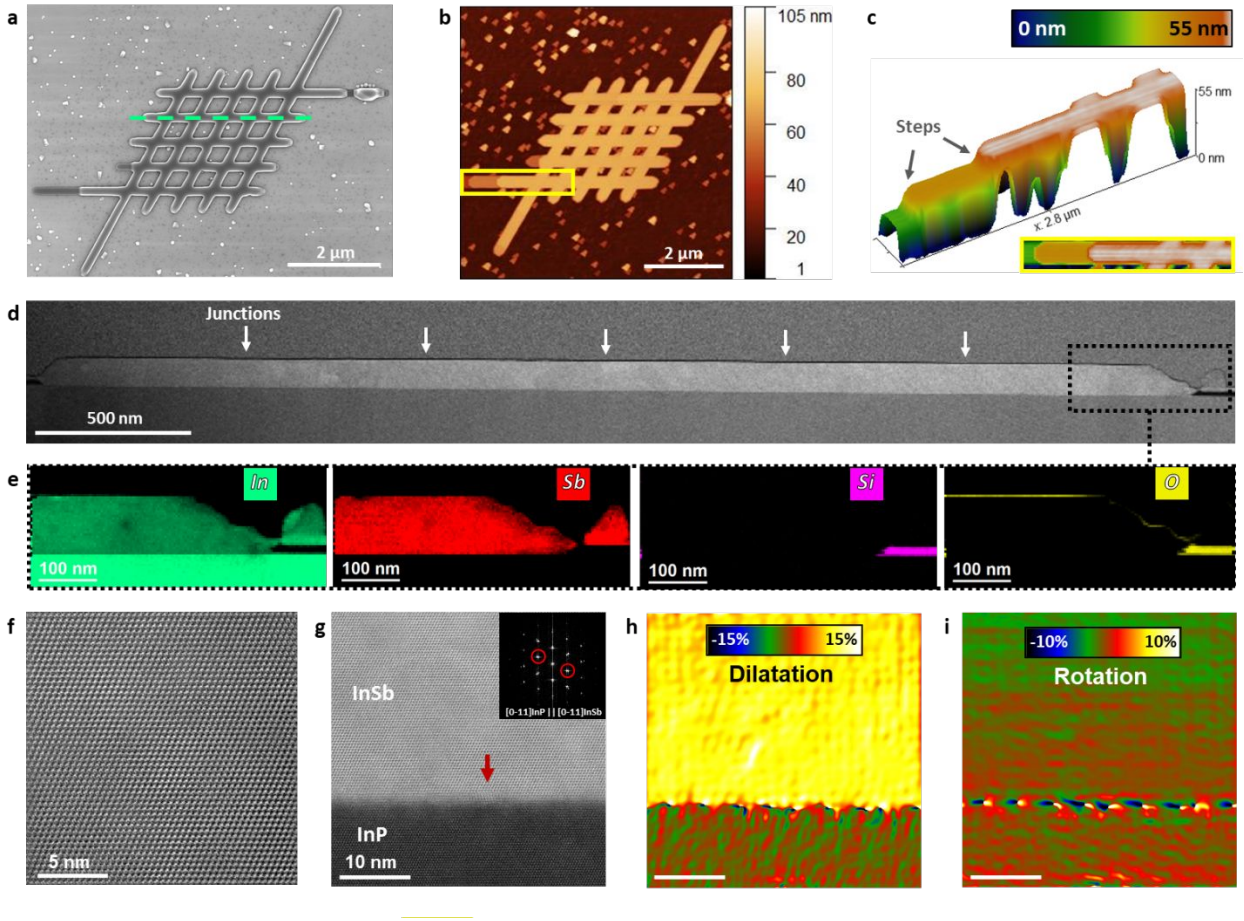

Figure 3. 5x5 InSb NW network on InP(111)B substrate with its morphology accessed by **(a)** SEM and **(b)** AFM with **(c)** the section highlighting the steps on its surface. Chemical composition of the similar network sliced through the 5 junctions (indicated by white arrows) observed by **(d)** HAADF and (**e)** EELS elemental maps. HAADF-STEM of **(f)** the top section of the InSb network and **(g)** InSb/InP interface containing partial twin plane (red arrow) with **(h)** dilatation and **(i)** rotation maps obtained through GPA applied to the peaks circled on a Fast Fourier Transform (FFT) power spectrum in the inset of panel **(g)**.

Out-of-plane morphology of a representative 5x5 InSb NW network with characteristic size of less than 7 μm (**Figure 3 a**) was accessed by atomic force microscopy (AFM) as shown in **Figure 3 b**. It reveals that the network's top facet is almost entirely atomically flat with only occasional large (>7nm in height) descending steps at the further end from the initial droplet position (**Figure 3 c**). No additional features were found around the NW junctions such as thickening or shape distortion previously observed in case of merging of out-of-plane NWs.[4]

Focused-ion beam (FIB) prepared lamella were cut longitudinally along $<11\bar{2}>$ direction through the 5x5 InSb NW network similar to the one shown in **Figure 3 a**. Excellent chemical uniformity across the entire cut was confirmed by the Z-contrast of high-angle annular dark-field (HAADF) imaging (**Figure 3 d**) and electron energy loss spectroscopy (EELS) elemental composition mapping (**Figure 3 e**). Atomic resolution HAADF-STEM imaging revealed a B-polar pure zincblende (ZB) crystal structure of InSb on the InP (111)B substrate (**Figure 3 f** and **S8 e-f**).[25] At the InSb/InP interface we observed formation of periodic array of in-plane misfit dislocations in both $<11\bar{2}>$ (**Figure 3 g, I** and **S8 c**) and $<1\bar{1}0>$ (**Figure S7 b**) directions.[26] Geometric Phase

Analysis (GPA) of the interface region (**Figure 3 h, i**) suggest that these defects are responsible for a full plastic strain relaxation of ~10.4% lattice mismatch between InSb and InP, as expected for largely mismatched III-V epitaxial systems.[9,10,12,27] Moreover, occasional horizontal single twin boundaries were observed in close (< 10nm) region to the InSb/InP interface (red arrow in **Figure 3 g**) as well as transverse 70.53° double twin boundaries (**Figure S8**), similarly to previously reported InAs SAG on InP(111)B substrate.[9] Additionally, we emphasize that we found no significant difference in structural nor chemical uniformity of NW junction regions compared to junction-free segments. Refer to **Supporting Information SE** for TEM examination of other wire orientations.

Having verified the structural quality of our InSb NWs and networks we now move to low-temperature electrical measurements to characterize the relevant scattering length scales in classical and quantum transport. After MBE growth, the wafer is diced into $5 \times 5\ \mathrm{mm}$ chips, each of which contains various semiconducting structures available for transport characterization devices. Ohmic contacts, dielectrics and gates are fabricated by standard means (**Supporting Information SF**). Devices are then cooled down in a dilution refrigerator with a base temperature of $T \sim 20\ \mathrm{mK}$. Measurements are performed

with standard DC + lock-in techniques at frequencies below 100 Hz in either voltage-biased or current-biased circuits.

Initial characterization is done by measuring the electron mobility defined in the Drude model for diffusive transport. We report on two types of strategies commonly employed in the literature to extract mobility using transport in one and two-dimensional nanostructures. The first is that of the classical Hall effect (**Figure 4a-d**) and the second is the long-channel field-effect transistor (FET) measurements (**Figure 4e,f**).

While Hall effect measurements have been the standard for two-dimensional materials, the planar device geometry required is not as easily achieved for NWs. Although Hall effect has been measured in InAs NWs by making use of the surface electron accumulation layer in that material,[28] electron depletion at InSb surfaces precludes similar attempts on InSb NWs.[29] Thus electron mobility in InSb NWs has been most commonly extracted either by taking the peak transconductance[30] or by fitting FET pinch-off curves.[31] Both Hall effect and field-effect methods assume the Drude model of conductance $\mu = \sigma/(ne)$ (μ,σ,n,e are mobility, conductivity, carrier density per volume and elementary charge, respectively). For both methods σ is measured directly, but n is

obtained differently for each method. Hall effect measurements give direct access to n via the Hall resistance R_{H} but field-effect measurements rely on estimation of n via $Q = e\mathcal{V}$ $n = CV_{\mathrm{g}}$. Here, C is the gate-to-device capacitance and V_{g} the gate voltage ($\mathcal{V}$ and Q are the volume of the semiconductor and total charge). A major drawback of this method is that only the product μC can be reliably extracted from a fit to the data. Acquiring an accurate estimation of μ then relies crucially on a reliable estimation of C (or Q), which is not trivial for nanodevices with non-ideal semiconductor-dielectric interfaces. However, the design flexibility of SAG allows us to easily overcome this drawback in straight NWs by fabricating NW Hall bars and measuring the carrier density via R_{H}, which does not rely on any C estimation and only requires NW width and length[32,33] as input parameters. Below, we first present such junction density and Hall mobility measurements assuming uniform electron sheet density throughout the Hall bar. The information obtained from this measurement then allows us to tune up a more detailed model of the device capacitance that includes local electron density variations and can be used for field-effect mobility estimations. Finally, comparison between mobilities obtained by the two methods are discussed.

Transport measurements in Hall-bar devices are shown in **Figure 4 a-d**. A $\sim$ 10 nA AC-current bias I_{bias} is applied as depicted in the circuit in **Figure 4a**. The longitudinal voltage response along the NW V_{xx} and the transverse voltage across a junction V_{xy} are measured using two synchronized lock-in amplifiers. Examples of the raw data taken during such a measurement are shown in **Supporting Information SG**. Using the Hall effect we extract the density n_{j} in the NW junction through $V_{xy} = I_{\mathrm{bias}} B_{\perp} / (n_{\mathrm{j,2D}} e)$, where $B_{\perp}$ is the applied out-of-plane magnetic field and $n_{\mathrm{j,2D}}$ the electron sheet density in the junction, defined as n_{j}/t with t being the NW thickness. By measuring V_{xy} and fitting it linearly in relation to the applied magnetic field, we obtain directly $n_{\mathrm{j,2D}}$. This measurement is repeated on each device at different $n_{\mathrm{j,2D}}$ values by tuning V_{g} (**Figure 4b**). Next, we can use the four-terminal conductivity along the NW $\sigma_{xx} = \frac{I_{\mathrm{bias}}}{V_{xx}} L_{xx} / (Wt)$, with ($L_{xx}$) the length of the channel and (W) the width, to determine the Hall mobility as $\mu_{\mathrm{H}} = \sigma_{xx} / (n_{\mathrm{j}} e)$ (**Figure 4c**). Strictly speaking, the estimation of mobility requires the channel density n_{c} in the straight wire segment instead of n_{j}. This inadequacy resulting from the uniform density assumption will be addressed below once we calibrate the electrostatic simulations with

the Hall measurement results and use it to model single NWs. As V_g increases, μ_H increases until it saturates at high positive V_g to value in the range $10{,}000 - 25{,}000$ cm^2 V^{-1} s^{-1}. Increased scattering at low n points towards a charged scattering,[34–36] with defects residing either in the NW interior or the semiconductor surfaces[37] and become better screened as n increases. At higher n, the saturation or slight decrease of μ is suggestive of surface roughness being the dominant scattering mechanism.[38,39] Such roughness and defects are known to occur in native InSb oxide surfaces[40,41] and become more relevant as the electron distribution gravitates towards the semiconductor-dielectric surface under positive gate voltages, as evidenced by our electrostatic simulations. Other factors including polar molecule adsorbants on InSb[31] and imperfections in the dielectric used may also contribute to the surface scattering. We can also calculate the mean free path, or the elastic scattering length, as $l_e = \mu\hbar k_F/e$, where $k_F = \sqrt{2\pi n_{2D}}$ is the two-dimensional Fermi wave vector. Assuming typical values of $n_{2D} \approx$ 1×10^{12} cm^{-2} and $\mu \approx$ 2×10^4 cm^2/(V s), we estimate $l_e \approx$ 330 nm. These results compare favorably with existing literature on InAs or InSb NW crosses produced by either SAG or VLS methods.[10,12,32,33] We would like to stress that as Hall effect measurements probe the transport properties inside the

NW cross junctions, the high mobility demonstrates the promising potential of our planar SAG approach in realizing advanced multi-terminal NW devices for topological quantum computing.[8,7,6]

In order to benchmark our MS SAG InSb NWs with their VLS-grown counterparts using the same method[31] and to compare transport in single wires and cross structures, we also measured field-effect mobility μ_{FE} in both single NWs and the Hall bars described above. In the former case, NW FETs (**Figure 4d**) are fabricated with contact spacing either L = 2 or 3 μm and a top gate that wraps around the transport region. For the latter we simply float the four transverse voltage probing arms of the NW Hall bars and perform two-terminal measurements from the left lead to the right lead. We measure current while varying V_{g} in both directions and fit the DC-conductance G with

$$G(V_{\mathrm{g}}) = \left[R_{\mathrm{s}} + \frac{L^2}{\mu_{\mathrm{FE}} Q_c(V_{\mathrm{g}})}\right]^{-1} \quad (1)$$

which takes as fitting parameters μ_{FE}, the total resistance in series with the transistor R_{s} and any unaccounted-for pinch-off threshold voltage ΔV_{th} by the simulated amount of charge $Q_c(V_{\mathrm{g}})$ accumulated in the transport channel as a function of V_{g}. Here, theoretical

modeling of the charge accumulation is achieved via 3D Thomas-Fermi (T-F) finite-element electrostatic simulations, which takes into account a layer of interface charge at the semiconductor-dielectric interface.[42,43] The T-F approximation is well applicable to high electron density regimes when the electron Fermi wavelength is smaller than the device width $\lambda_{\mathrm{F}} < W$.[42] The interface charge density D_{it} is obtained by setting it as a fitting parameter while calibrating the model of the NW cross on the Hall-bar charge density measurement results shown in **Figure 4c**. The fitted values of D_{it} for the 6 Hall bars ranges from 0.8×10^{12} cm^{-2} eV^{-1} to 6.8×10^{12} cm^{-2} eV^{-1} with the average being 2.9×10^{12} cm^{-2} eV^{-1}, similar to experimental findings of the quantity on InAs NW transistors in reference.[44] In the case of linear charge accumulation $Q = C(V_{\mathrm{g}} - \Delta V_{\mathrm{th}})$ and $D_{\mathrm{it}} = 0$, this method reduces to the standard literature apporach.[31] Due to different surface to volume ratios and the gate geometry, we observe typically different electron density in the junction (n_{j}) and in the straight channel (n_{c}) for NW Hall bars. The translation from n_{j} to n_{c} (and thus Q_c of the FET devices) and other details of the model are described in the **Supporting Information SH**. The example of such a pinch-off curve and the device on which it was measured,

together with the simulated charge area density by our theoretical model, are shown in **Figure 4e**.

We have thus measured sixteen FETs and the results are summarized in **Figure 4f**. The averaged field-effect mobility $\bar{\mu}_{\mathrm{FE}} = 1.9 \pm 0.6 \times 10^4\ \mathrm{cm}^2\,\mathrm{V}^{-1}\mathrm{s}^{-1}$ for upward gate sweeps, agreeing roughly with μ_{H} data. The μ_{FE} measured on NW Hall bars are displayed in **Figure 4d** as horizontal lines spanning the gate range in which they are measured. The difference between μ_{FE} and μ_{H} may be attributed to the fact that they do not reflect transport properties in the exact same regions in the device. Where μ_{FE} is measured between the normal contacts, μ_{H} is measured only between the voltage probes of the Hall bar. Furthermore, hysteresis in pinch-off curves and the finite surface charge density required to match simulations with the measured n indicate the presence of a dynamic surface charge density at the semiconductor-dielectric interface, which complicates the comparison. However, we observe that the extracted μ_{FE} of single NWs, of entire Hall bars and μ_{H} are all in a similar range, which would mean that the cross junctions do not disproportionately add more scattering. Such cross junctions are crucial ingredients for

integration of parity read out needed for measurement-based braiding of Majorana zero modes.[8,7,6]

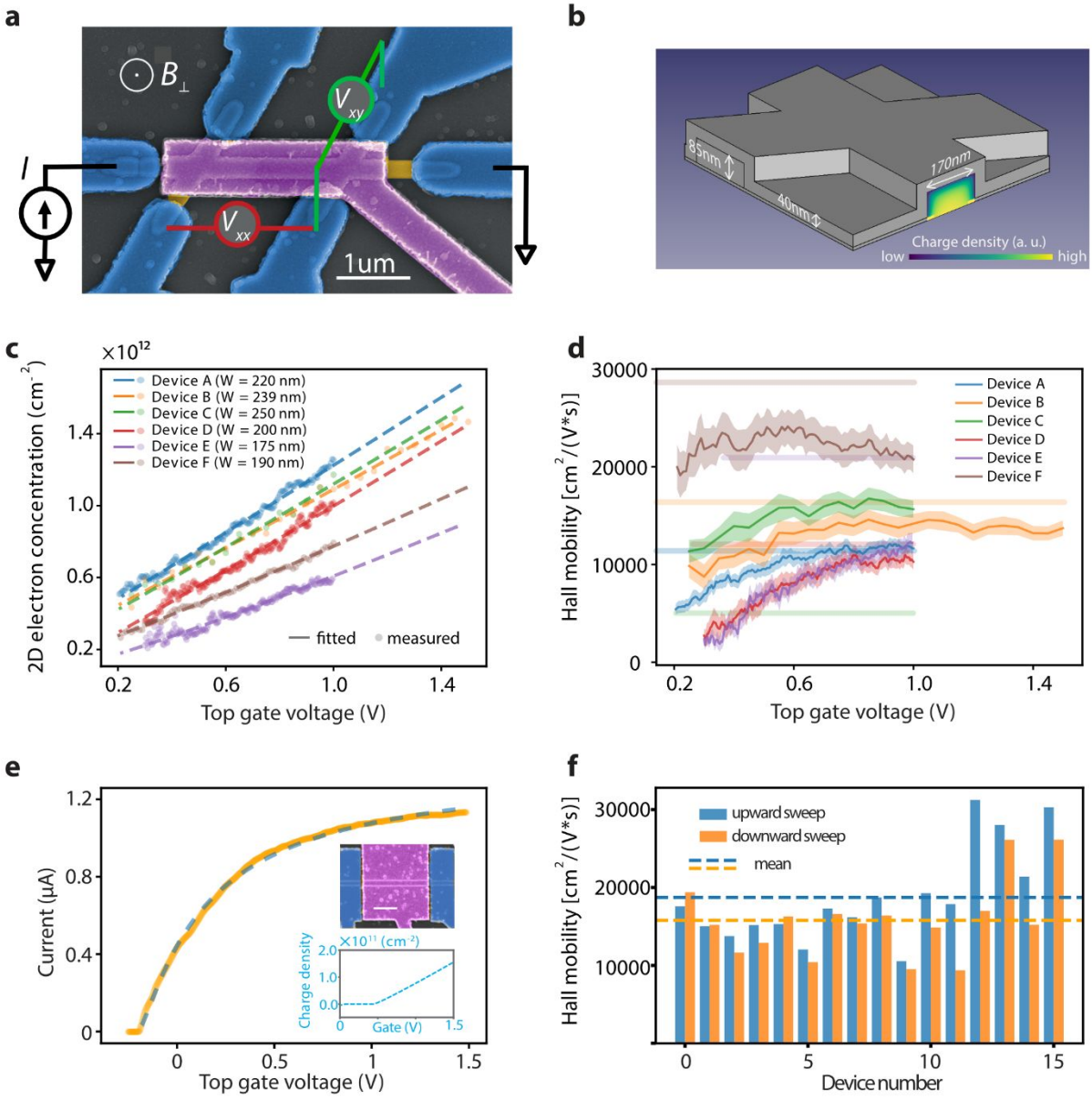

Figure 4. Diffusive transport properties of NWs and junctions demonstrating high electron mobility in both Hall effect and field-effect transistor measurements. **(a)** False-colored SEM image of a Hall bar measured

(Device C) with illustration of the four-terminal circuit used for Hall effect measurements. Blue regions mark the Cr/Au Ohmic contacts evaporated on top of the sulphur-passivated surface of InSb. The purple region marks the gate electrode, separated from the NW by a layer of SiN_x dielectric (not visible) sputtered globally onto the entire chip. Blue is the NW. The scale bar is 1 μm. **(b)** View of the NW model used for electrostatic simulation of the Hall bar junctions. The potential profile is simulated for the NW-cross region depicted assuming appropriate material parameters and with input from the Hall measurements to establish the surface charge density. The tiled inset shows an example of the calculated electron density profile in the cross section. **(c)** Carrier concentration of the 6 NW Hall bars obtained from classical Hall effect measurements via $n_{2\mathrm{D}} = (e\Delta R_{\mathrm{H}}/\Delta B)^{-1}$, together with the calibrated simulation result of them. **(d)** Hall mobility calculated from carrier concentration and sample resistivity obtained by Hall measurements described above according to $\sigma = ne\mu$. Horizontal lines in each color represent the corresponding field-effect mobility on each device. **(e)** An example pinch-off curve (orange) of the FET device used for field-effect mobility extraction and its SEM image shown in the top inset (scale bar is 1). A DC bias voltage $V_{\mathrm{bias}} =$ 10 mV is applied between source and drain contacts (blue). G is measured while applying V_{g} to the gate (pink). Blue dashed lines are best fits of Eq. (1) to the data from which we extract μ. **(f)** Field effect mobility of all NW FETs measured. All curves were taken by sweeping the gate both from below pinch-off to saturation (upwards) and in the opposite direction (downwards). Horizontal dashed lines indicate the averaged mobility of all devices in both directions.

With the mobilities we observed in long channels, we set out to measurement of NW quantum point contacts (QPCs) and confirm ballistic transport in our InSb MS SAG NWs.[4,45–47] Indeed we observe ballistic transport in such a single NW QPC device with 440 ± 20 nm contact spacing (**Figure 5a-d**), as well as in other devices (**Supporting Information SI**). We measure the differential conductance of the device shown in **Figure 5a** as a function of DC-V_{bias}, V_{g} and $B_{\parallel}$. **Figure 5b** shows pinch-off traces taken at $V_{\mathrm{bias}} = 0\ \mathrm{V}$ in DC under increasing $B_{\parallel}$ from left to right (offset horizontally for clarity). A conductance plateau at $G_0 = 2e^2/h$ begins to emerge at around $B_{\parallel} = 1.2\ \mathrm{T}$ as cyclotron orbits gradually suppress backscattering.[45] More plateaus appear at higher fields and at other multiples of $0.5G_0$ as Zeeman splitting lifts the electron spin degeneracy of the subbands. The red linecut at $B_{\parallel} = 3.9\ \mathrm{T}$ show conductance plateaus of the first, third and fifth spin-split subbands. We attribute slight deviations of the plateaus from half-integer multiples of G_0 to unaccounted-for contact resistance.

We investigate the evolution of the conductance plateaus with $B_{\parallel}$ (**Figure 5c**). For higher $B_{\parallel}$, the plateaus widen and become more clear as spin splitting becomes larger. At around $B_{\parallel} = 3.9\ \mathrm{T}$, the higher-energy spin subband of the lowest orbital ($E_{1\uparrow}$) crosses

the lower-energy spin subband of the second orbital ($E_{2\downarrow}$), rendering the $1G_0$ plateau too narrow to distinguish until $B_\parallel > 5\,\mathrm{T}$ when it re-emerges after the crossing. As for $B_\parallel < 1.2\,\mathrm{T}$, clear plateau features become obscured by mesoscopic conductance fluctuations which can be attributed to backscattering as a result of uncontrolled potentials induced by non-gated section of the transport channel and/or by the contacts to the semiconductor.

Bias spectroscopy taken at $B_\parallel = 3\,\mathrm{T}$ (**Figure 5d**) further reveals relevant energy scales via diamond-shaped conductance plateaus of the first few spin-split subbands.[45,46] The $0.5G_0$ plateau vanishes at $V_{\mathrm{bias}} \approx 8\,\mathrm{mV}$ when the chemical potential difference between the two leads is equal to the energy splitting between the first two spin-split subbands.[48–50] The relation $eV_{\mathrm{bias}} = E_{1\uparrow} - E_{1\downarrow} = g\mu_{\mathrm{B}}B_\parallel$, where μ_{B} is the Bohr magneton, allows us to extract a Landé g-factor of $g \sim 46$, in accordance with previous observations in InSb VLS NWs.[45,51,52] The subband spacing between the first two spin-degenerate orbitals is similarly calculated by summing the width of the first two diamonds to be $\sim 12\,\mathrm{meV}$. We consistently observe ballistic transport on length scales of several hundred nm in multiple InSb MS SAG QPC devices (**Supporting Information SI**).

With ballistic transport established in InSb MS SAG, we finally move to demonstrate phase coherent transport and extraction of inelastic scattering length, a.k.a. phase coherence length (**Figure 5e-g**) by a quantum interference experiment. Crucially, this requires the ability to grow high-quality networks as demonstrated in **Figure 2**. Such networks are requisite ingredients for implementing proposals for manipulating Majorana states via electron teleportation[8] and for making topological qubits,[6,7] provided electrons retain their memory of the quantum mechanical phase throughout the structure. The canonical experiment for proving phase-coherent transport is by measuring the conductance of a semiconducting loop modulated by Aharonov-Bohm (AB) interference (**Figure 5e**).[4,53] In such magnetoconductance measurements the two-terminal conductance is probed from one side of the loop, with surface area A, to the other while it is threaded by a flux $\Phi = B_{\perp} A$. If the transport is phase coherent, the applied flux induces conductance oscillations as a result of the quantum interference between electron trajectories passing through the two arms of the loop. The periodicity of the oscillations depends on the loop area A and the magnetic flux quantum $\Phi_0 = h/e$ as $\Delta B_{\perp} = \Phi_0/A$.

Figure 5f plots two representative magnetoconductance measurement results in MS SAG Aharonov-Bohm (AB) loop devices. We observe higher frequency oscillations superimposed on an irregular slow-varying background of mesoscopic conductance fluctuations. After subtracting the background, the conductance clearly exhibits periodic oscillations as shown in the example in the inset of **Figure 5f**. Such magnetoconductance traces are then taken with the device depicted in **Figure 5e** for several values of V_{g} and their Fourier spectra are averaged to reveal a clear peak at the expected frequency in **Figure 5f**. Its second harmonic is also visible in the spectrum, which results from AB interference between electron paths of opposite directions traversing the entire loop. The peak broadening can be explained by the finite width of the wire, which sets upper and lower bounds on the periodicity. The expected bounds coincide well with the observed peak.

We can extract the electron phase coherence length l_ϕ in our devices by measuring the temperature dependence of the first harmonic peak amplitude. In the case of diffusive transport, the peak amplitude is expected to follow the relation $A_{h/e} = A_0 \exp\left(-a\sqrt{T}\right)$ where A_0 and a are fitting parameters and the phase coherence length is described in

these terms as $l_\phi = \frac{L}{a\sqrt{T}}$ with L being the loop circumference.[54,55] We measure AB oscillations in the same range of magnetic field at different temperatures on the device shown in **Figure 5e** and fit the first-harmonic peak in each Fourier spectrum with a Gaussian envelope. The peak amplitudes thus obtained are then fitted with A_0,a as parameters and the resulting l_ϕ dependence on temperature is plotted as the orange dashed line in **Figure 5g**. To visualize the standard deviation of the fitting procedure, we translate the oscillation amplitude at each measured temperature back into a decoherence length scale and plot them in the same panel together with the fitting standard deviation. The phase coherence thus extracted is about 7.5 μm at 50 mK, the measured electron temperature in our fridge.

In summary, we have demonstrated the Metal-Sown Selective Area Growth technique to overcome the challenge of non-overlapping nucleation and selective growth conditions and applied it to InSb heteroepitaxy. This is achieved by selective group III adatoms pre-deposition at selectivity favoring conditions and its subsequent conversion into III-V crystal under group V flux at nucleation favoring conditions. We have successfully

obtained complex InSb nanowire networks and accessed confirmed their high structural quality by transmission electron microscopy. Consistently high mobility values are extracted by both Hall and field effect techniques in the presence of cross junctions. The materials quality was verified by the observation of ballistic transport with conductance plateaus up to the fifth spin-split subband and a long phase coherence length of 7.5 μm. The results point at promising applications of InSb nanowire networks to advanced topological hybrid semiconducting/ superconducting networks.

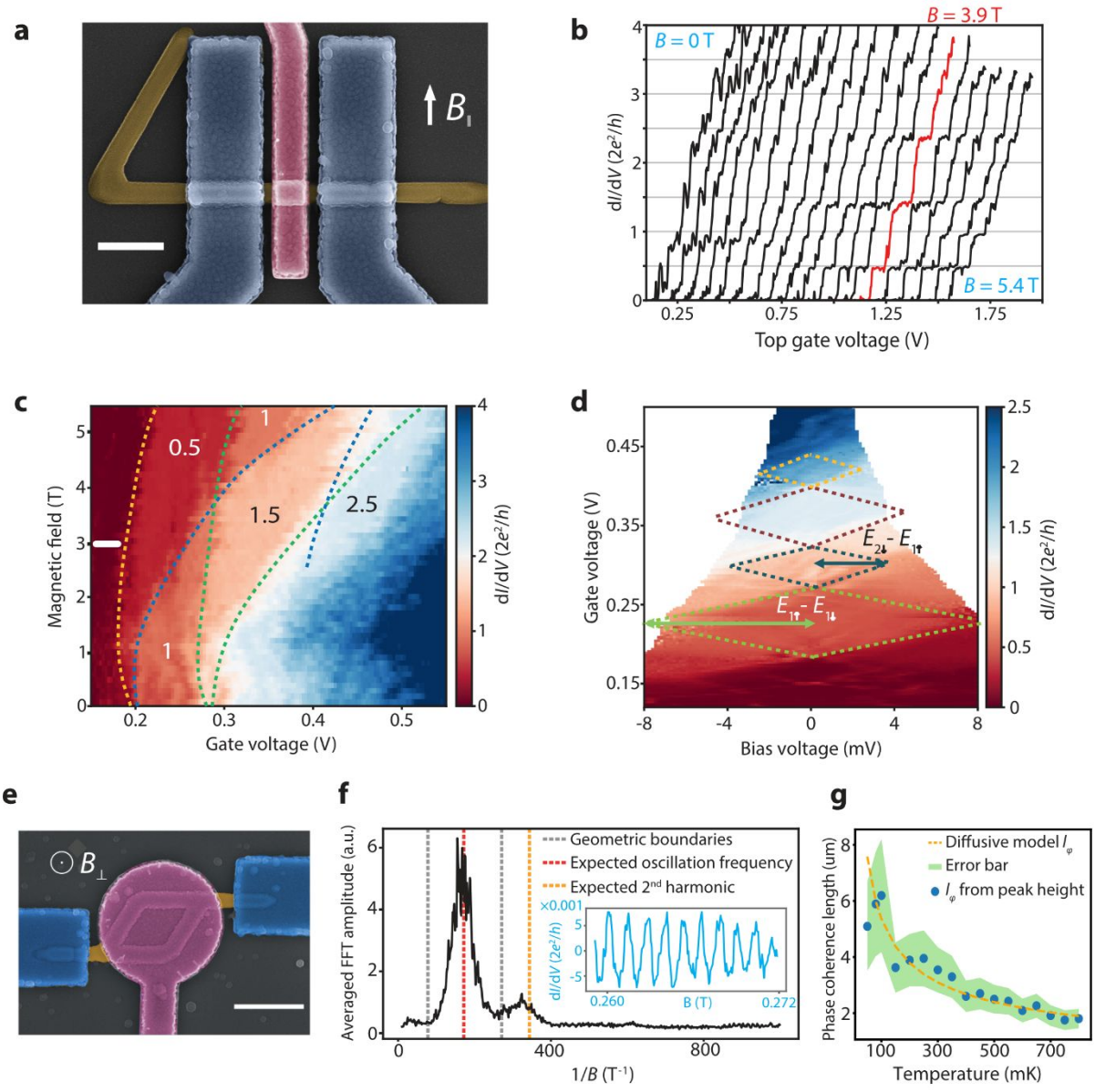

Figure 5. Ballistic transport under finite magnetic field in an InSb quantum point contact and phase coherent transport in a NW loop. **(a)** False-colored SEM image of the InSb QPC device. Contacts are in blue, gate in purple and NW in blue. Scale bar is 500 nm. Magnetic field is applied along the in-plane direction perpendicular to the NW. **(b)** Zero-DC-bias pinch-off traces of the device shown in (a), taken at field values between 0 and 5.5 T with intervals of 0.3 T. Each curve is shifted horizontally from the previous one by

+75 mV for clarity. Highlighted curve at 3.9 T shows the first, third and fifth spin-split conductance plateaus. **(c)** Plot of zero-DC-bias conductance under different gate and magnetic field showing the evolution of subband plateaus as increasing B gradually suppresses backscattering and increases the splitting between the two spin subbands. Dashed lines are guides to the eyes separating conductance plateaus. **(d)** Differential conductance measured as a function of V_{bias} and gate voltages showing the first few spin-split subbands, taken at a magnetic field of 3 T (indicated in panel **(c)** by a white line). The diamond shapes in the color plot provide information on the g-factor and subband spacing in the NW as indicated by the labels. **(e)** Top-view SEM image of one of the InSb NW loops in which Aharanov-Bohm conductance oscillations were observed. Ohmic contacts are marked in blue and the wrapping gate in purple. The circumference of the loop measured along the geometrical center of the NW is 4. The scale bar is 800 nm. Magnetic field is applied perpendicular to the loop. The area enclosed by the NW center is measured to be 0.69 μm^2. **(f)** Averaged fast-Fourier-transform spectrum of magnetoconductance traces of the device in (a) among different gate voltages, after subtraction of a low-frequency background. The red line identifies the peak corresponding to the magnetic field periodicity given by a flux quantum through the area of the loop. Grey lines denote the expected widening of the signal peak due to the finite width of the NW. The second harmonic peak is identified by the orange line. Inset: the magnetoconductance trace of another loop with a larger size (circumference 8 μm, area 3.25 μm^2) after subtraction of background. **(g)** Temperature dependence of the extracted phase-coherence length as the orange dashed line, together with the fitting

errors and the measured oscillation amplitudes translated into length scales according to the fitting formula as scattered dots.

ASSOCIATED CONTENT

Supporting Information.

The supporting information is available free of charge on the website.

Additional details and figures on InSb MS SAG on GaAs(001) substrates, demonstration of trials of conventional SAG of InSb, RHEED oscillation during planar InSb growth, In droplet induced damage to the mask, and strain relaxation in InSb MS SAG on InP(111)B substrates. Device fabrication details, examples of Hall effect measurements, details on electrostatics simulations, and all other QPC plateaus observed in measurements are given as well (PDF).

AUTHOR INFORMATION

† – these authors contributed equally

Corresponding Authors

* E-mail: Pavel.Aseev@microsoft.com

* E-mail: Philippe.Caroff@microsoft.com

Author Contributions

P.A. conceived the idea for the research as well as performed the growth, growth kinetic studies, morphological analysis and wrote the corresponding part of the manuscript. G. W., and L. B. fabricated devices and performed their electronic characterization and analysis and G. W. wrote the corresponding part of the manuscript. A. S. developed mask preparation procedure and provided patterned substrates for the growth. L.J. S., A. B., and J. D. W. assisted with device fabrication and electronic measurements. S. M.-S., M. B. and J. A. performed TEM sample preparation and related structural and compositional analyses as well as wrote the corresponding section of the manuscript. D. A., J. G., K. v. H. developed computational model for mobility curves fitting. F. B. participated in the growth discussion and assisted with the growth. P. C., G.d. L., and L. P. K. supervised the work and provided extensive comments to the manuscript. All authors commented on the work and provided valuable input throughout the project as well as approved the final version of the manuscript.

Funding Sources

Notes

The authors declare no competing financial interest.

ACKNOWLEDGMENT

The project was supported by Microsoft Station Q (Delft). P.A. and P.C. gratefully acknowledges Emrah Yucelen for fruitful discussions on transmission electron microscopy study. S.M.-S acknowledges funding from "Programa Internacional de Becas "la Caixa"-Severo Ochoa". ICN2 members acknowledge funding from Generalitat de Catalunya 2017 SGR 327. ICN2 acknowledges support from the Severo Ochoa Programme (MINECO, Grant no. SEV-2013-0295) and is funded by the CERCA Programme / Generalitat de Catalunya. Part of the present work has been performed in the framework of Universitat Autònoma de Barcelona Materials Science PhD program. Part of the HAADF-STEM microscopy was conducted in the Laboratorio de Microscopias Avanzadas at Instituto de Nanociencia de Aragon-Universidad de Zaragoza. ICN2 acknowledge support from CSIC Research Platform on Quantum Technologies PTI-001.

REFERENCES

(1) Kitaev, A. Yu. Fault-Tolerant Quantum Computation by Anyons. *Ann. Phys.* **2003**, *303* (1), 2–30. https://doi.org/10.1016/S0003-4916(02)00018-0.

(2) van Weperen, I.; Tarasinski, B.; Eeltink, D.; Pribiag, V. S.; Plissard, S. R.; Bakkers, E. P. A. M.; Kouwenhoven, L. P.; Wimmer, M. Spin-Orbit Interaction in InSb Nanowires. *Phys. Rev. B* **2015**, *91* (20). https://doi.org/10.1103/PhysRevB.91.201413.

(3) Zhang, H.; Liu, C.-X.; Gazibegovic, S.; Xu, D.; Logan, J. A.; Wang, G.; van Loo, N.; Bommer, J. D. S.; de Moor, M. W. A.; Car, D.; et al. Quantized Majorana Conductance. *Nature* **2018**, *556*, 74.

(4) Gazibegovic, S.; Car, D.; Zhang, H.; Balk, S. C.; Logan, J. A.; de Moor, M. W. A.; Cassidy, M. C.; Schmits, R.; Xu, D.; Wang, G.; et al. Epitaxy of Advanced Nanowire Quantum Devices. *Nature* **2017**, *548*, 434.

(5) Lutchyn, R. M.; Bakkers, E. P. A. M.; Kouwenhoven, L. P.; Krogstrup, P.; Marcus, C. M.; Oreg, Y. Majorana Zero Modes in Superconductor–Semiconductor Heterostructures. *Nat. Rev. Mater.* **2018**, *3* (5), 52–68. https://doi.org/10.1038/s41578-018-0003-1.

(6) Karzig, T.; Knapp, C.; Lutchyn, R. M.; Bonderson, P.; Hastings, M. B.; Nayak, C.; Alicea, J.; Flensberg, K.; Plugge, S.; Oreg, Y.; et al. Scalable Designs for Quasiparticle-Poisoning-Protected Topological Quantum Computation with Majorana Zero Modes. *Phys. Rev. B* **2017**, *95* (23). https://doi.org/10.1103/PhysRevB.95.235305.

(7) Plugge, S.; Rasmussen, A.; Egger, R.; Flensberg, K. Majorana Box Qubits. *New J. Phys.* **2017**, *19* (1), 012001. https://doi.org/10.1088/1367-2630/aa54e1.

(8) Fu, L. Electron Teleportation via Majorana Bound States in a Mesoscopic Superconductor. *Phys. Rev. Lett.* **2010**, *104* (5), 056402. https://doi.org/10.1103/PhysRevLett.104.056402.

(9) Aseev, P.; Fursina, A.; Boekhout, F.; Krizek, F.; Sestoft, J. E.; Borsoi, F.; Heedt, S.; Wang, G.; Binci, L.; Martí-Sánchez, S.; et al. Selectivity Map for Molecular Beam Epitaxy of Advanced III–V Quantum Nanowire Networks. *Nano Lett.* **2019**, *19* (1), 218–227. https://doi.org/10.1021/acs.nanolett.8b03733.

(10) Krizek, F.; Sestoft, J. E.; Aseev, P.; Marti-Sanchez, S.; Vaitiekėnas, S.; Casparis, L.; Khan, S. A.; Liu, Y.; Stankevič, T.; Whiticar, A. M.; et al. Field Effect Enhancement in Buffered Quantum Nanowire Networks. *Phys. Rev. Mater.* **2018**, *2* (9). https://doi.org/10.1103/PhysRevMaterials.2.093401.

(11) Friedl, M.; Cerveny, K.; Weigele, P.; Tütüncüoglu, G.; Martí-Sánchez, S.; Huang, C.; Patlatiuk, T.; Potts, H.; Sun, Z.; Hill, M. O.; et al. Template-Assisted Scalable

Nanowire Networks. *Nano Lett.* **2018**, *18* (4), 2666–2671. https://doi.org/10.1021/acs.nanolett.8b00554.

(12) Desplanque, L.; Bucamp, A.; Troadec, D.; Patriarche, G.; Wallart, X. In-Plane InSb Nanowires Grown by Selective Area Molecular Beam Epitaxy on Semi-Insulating Substrate. *Nanotechnology* **2018**, *29* (30), 305705. https://doi.org/10.1088/1361-6528/aac321.

(13) Desplanque, L.; Bucamp, A.; Troadec, D.; Patriarche, G.; Wallart, X. Selective Area Molecular Beam Epitaxy of InSb Nanostructures on Mismatched Substrates. *J. Cryst. Growth* **2019**, *512*, 6–10. https://doi.org/10.1016/j.jcrysgro.2019.02.012.

(14) Michel, E.; Singh, G.; Slivken, S.; Besikci, C.; Bove, P.; Ferguson, I.; Razeghi, M. Molecular Beam Epitaxial Growth of High Quality InSb. *Appl. Phys. Lett.* **1994**, *65* (26), 3338–3340. https://doi.org/10.1063/1.112384.

(15) Hara, S.; Iida, T.; Nishino, Y.; Uchida, A.; Horii, H.; Fujishiro, H. I. Selective Growth of InSb on Localized Area of Si(100) by Molecular Beam Epitaxy. *J. Cryst. Growth* **2011**, *323* (1), 397–400. https://doi.org/10.1016/j.jcrysgro.2010.11.134.

(16) Kanisawa, K.; Yamaguchi, H.; Hirayama, Y. Two-Dimensional Growth of InSb Thin Films on GaAs(111)A Substrates. *Appl. Phys. Lett.* **2000**, *76* (5), 589–591. https://doi.org/10.1063/1.125826.

(17) Ferguson, I. T.; de Oliveira, A. G.; Joyce, B. A. RHEED Intensity Effects during the Growth of InAs, InSb and In(As,Sb) by Molecular Beam Epitaxy. *J. Cryst. Growth* **1992**, *121* (3), 267–277. https://doi.org/10.1016/0022-0248(92)90137-8.

(18) Fortuna, S. A.; Wen, J.; Chun, I. S.; Li, X. Planar GaAs Nanowires on GaAs (100) Substrates: Self-Aligned, Nearly Twin-Defect Free, and Transfer-Printable. *Nano Lett.* **2008**, *8* (12), 4421–4427. https://doi.org/10.1021/nl802331m.

(19) Fonseka, H. A.; Caroff, P.; Wong-Leung, J.; Ameruddin, A. S.; Tan, H. H.; Jagadish, C. Nanowires Grown on InP (100): Growth Directions, Facets, Crystal Structures, and Relative Yield Control. *ACS Nano* **2014**, *8* (7), 6945–6954. https://doi.org/10.1021/nn5017428.

(20) Zhang, C.; Miao, X.; Mohseni, P. K.; Choi, W.; Li, X. Site-Controlled VLS Growth of Planar Nanowires: Yield and Mechanism. *Nano Lett.* **2014**, *14* (12), 6836–6841. https://doi.org/10.1021/nl502525z.

(21) Zhang, C.; Miao, X.; Chabak, K. D.; Li, X. A Review of III–V Planar Nanowire Arrays: Selective Lateral VLS Epitaxy and 3D Transistors. *J. Phys. Appl. Phys.* **2017**, *50* (39), 393001. https://doi.org/10.1088/1361-6463/aa7e42.

(22) Gurioli, M.; Wang, Z.; Rastelli, A.; Kuroda, T.; Sanguinetti, S. Droplet Epitaxy of Semiconductor Nanostructures for Quantum Photonic Devices. *Nat. Mater.* **2019**. https://doi.org/10.1038/s41563-019-0355-y.

(23) Bietti, S.; Somaschini, C.; Esposito, L.; Fedorov, A.; Sanguinetti, S. Gallium Surface Diffusion on GaAs (001) Surfaces Measured by Crystallization Dynamics of Ga Droplets. *J. Appl. Phys.* **2014**, *116* (11), 114311. https://doi.org/10.1063/1.4895986.

(24) Stevens, M. A.; Tomasulo, S.; Maximenko, S.; Vandervelde, T. E.; Yakes, M. K. Surface Diffusion Measurements of In on InGaAs Enabled by Droplet Epitaxy. *J. Appl. Phys.* **2017**, *121* (19), 195302. https://doi.org/10.1063/1.4983257.

(25) de la Mata, M.; Magen, C.; Gazquez, J.; Utama, M. I. B.; Heiss, M.; Lopatin, S.; Furtmayr, F.; Fernández-Rojas, C. J.; Peng, B.; Morante, J. R.; et al. Polarity Assignment in ZnTe, GaAs, ZnO, and GaN-AlN Nanowires from Direct Dumbbell Analysis. *Nano Lett.* **2012**, *12* (5), 2579–2586. https://doi.org/10.1021/nl300840q.

(26) de la Mata, M.; Magén, C.; Caroff, P.; Arbiol, J. Atomic Scale Strain Relaxation in Axial Semiconductor III–V Nanowire Heterostructures. *Nano Lett.* **2014**, *14* (11), 6614–6620. https://doi.org/10.1021/nl503273j.

(27) Kanungo, P. D.; Schmid, H.; Björk, M. T.; Gignac, L. M.; Breslin, C.; Bruley, J.; Bessire, C. D.; Riel, H. Selective Area Growth of III–V Nanowires and Their Heterostructures on Silicon in a Nanotube Template: Towards Monolithic Integration of Nano-Devices. *Nanotechnology* **2013**, *24* (22), 225304. https://doi.org/10.1088/0957-4484/24/22/225304.

(28) Blömers, Ch.; Grap, T.; Lepsa, M. I.; Moers, J.; Trellenkamp, St.; Grützmacher, D.; Lüth, H.; Schäpers, Th. Hall Effect Measurements on InAs Nanowires. *Appl. Phys. Lett.* **2012**, *101* (15), 152106. https://doi.org/10.1063/1.4759124.

(29) King, P. D. C.; Veal, T. D.; Lowe, M. J.; McConville, C. F. Surface Electronic Properties of Clean and S-Terminated InSb(001) and (111)B. *J. Appl. Phys.* **2008**, *104* (8), 083709. https://doi.org/10.1063/1.3000567.

(30) Schroder, D. K. *Semiconductor Material and Device Characterization: Schroder/Semiconductor Material and Device Characterization, Third Edition*; John Wiley & Sons, Inc.: Hoboken, NJ, USA, 2005. https://doi.org/10.1002/0471749095.

(31) Gül, Ö.; Woerkom, D. J. van; Weperen, I. van; Car, D.; Plissard, S. R.; Bakkers, E. P. A. M.; Kouwenhoven, L. P. Towards High Mobility InSb Nanowire Devices. *Nanotechnology* **2015**, *26* (21), 215202. https://doi.org/10.1088/0957-4484/26/21/215202.

(32) Lee, J. S.; Choi, S.; Pendharkar, M.; Pennachio, D. J.; Markman, B.; Seas, M.; Koelling, S.; Verheijen, M. A.; Casparis, L.; Petersson, K. D.; et al. Selective-Area Chemical Beam Epitaxy of in-Plane InAs One-Dimensional Channels Grown on InP(001), InP(111)B, and InP(011) Surfaces. *Phys. Rev. Mater.* **2019**, *3* (8). https://doi.org/10.1103/PhysRevMaterials.3.084606.

(33) Plissard, S. R.; van Weperen, I.; Car, D.; Verheijen, M. A.; Immink, G. W. G.; Kammhuber, J.; Cornelissen, L. J.; Szombati, D. B.; Geresdi, A.; Frolov, S. M.; et al. Formation and Electronic Properties of InSb Nanocrosses. *Nat. Nanotechnol.* **2013**, *8* (11), 859–864. https://doi.org/10.1038/nnano.2013.198.

(34) Ando, T.; Fowler, A. B.; Stern, F. Electronic Properties of Two-Dimensional Systems. *Rev. Mod. Phys.* **1982**, *54* (2), 437–672. https://doi.org/10.1103/RevModPhys.54.437.

(35) Das Sarma, S.; Hwang, E. H. Universal Density Scaling of Disorder-Limited Low-Temperature Conductivity in High-Mobility Two-Dimensional Systems. *Phys. Rev. B* **2013**, *88* (3). https://doi.org/10.1103/PhysRevB.88.035439.

(36) Umansky, V.; de-Picciotto, R.; Heiblum, M. Extremely High-Mobility Two Dimensional Electron Gas: Evaluation of Scattering Mechanisms. *Appl. Phys. Lett.* **1997**, *71* (5), 683–685. https://doi.org/10.1063/1.119829.

(37) Pauka, S. J.; Witt, J. D. S.; Allen, C. N.; Harlech-Jones, B.; Jouan, A.; Gardner, G. C.; Gronin, S.; Wang, T.; Thomas, C.; Manfra, M. J.; et al. Repairing the Surface of InAs-Based Topological Heterostructures. *ArXiv190808689 Cond-Mat* **2019**.

(38) Chung, S. J.; Goldammer, K. J.; Lindstrom, S. C.; Johnson, M. B.; Santos, M. B. Study of Factors Limiting Electron Mobility in InSb Quantum Wells. *J. Vac. Sci.*

Technol. B Microelectron. Nanometer Struct. **1999**, *17* (3), 1151. https://doi.org/10.1116/1.590712.

(39) Fu, H.; Reich, K. V.; Shklovskii, B. I. Surface Roughness Scattering in Multisubband Accumulation Layers. *Phys. Rev. B* **2016**, *93* (23). https://doi.org/10.1103/PhysRevB.93.235312.

(40) Mäkelä, J.; Jahanshah Rad, Z. S.; Lehtiö, J.-P.; Kuzmin, M.; Punkkinen, M. P. J.; Laukkanen, P.; Kokko, K. Crystalline and Oxide Phases Revealed and Formed on InSb(111)B. *Sci. Rep.* **2018**, *8* (1). https://doi.org/10.1038/s41598-018-32723-5.

(41) Webb, J. L.; Knutsson, J.; Hjort, M.; Gorji Ghalamestani, S.; Dick, K. A.; Timm, R.; Mikkelsen, A. Electrical and Surface Properties of InAs/InSb Nanowires Cleaned by Atomic Hydrogen. *Nano Lett.* **2015**, *15* (8), 4865–4875. https://doi.org/10.1021/acs.nanolett.5b00282.

(42) Ihn, T. *Electronic Quantum Transport in Mesoscopic Semiconductor Structures*; Höhler, G., Kühn, J., Müller, T., Ruckenstein, A., Steiner, F., Trümper, J., Wölfle, P., Series Eds.; Springer Tracts in Modern Physics; Springer New York: New York, NY, 2004; Vol. 192. https://doi.org/10.1007/b97630.

(43) Sze, S. M.; Ng, K. K. *Physics of Semiconductor Devices: Sze/Physics*; John Wiley & Sons, Inc.: Hoboken, NJ, USA, 2006. https://doi.org/10.1002/0470068329.

(44) Heedt, S.; Otto, I.; Sladek, K.; Hardtdegen, H.; Schubert, J.; Demarina, N.; Lüth, H.; Grützmacher, D.; Schäpers, T. Resolving Ambiguities in Nanowire Field-Effect Transistor Characterization. *Nanoscale* **2015**, *7* (43), 18188–18197. https://doi.org/10.1039/C5NR03608A.

(45) van Weperen, I.; Plissard, S. R.; Bakkers, E. P. A. M.; Frolov, S. M.; Kouwenhoven, L. P. Quantized Conductance in an InSb Nanowire. *Nano Lett.* **2013**, *13* (2), 387–391. https://doi.org/10.1021/nl3035256.

(46) Kammhuber, J.; Cassidy, M. C.; Zhang, H.; Gül, Ö.; Pei, F.; de Moor, M. W. A.; Nijholt, B.; Watanabe, K.; Taniguchi, T.; Car, D.; et al. Conductance Quantization at Zero Magnetic Field in InSb Nanowires. *Nano Lett.* **2016**, *16* (6), 3482–3486. https://doi.org/10.1021/acs.nanolett.6b00051.

(47) Gül, Ö.; Zhang, H.; Bommer, J. D. S.; de Moor, M. W. A.; Car, D.; Plissard, S. R.; Bakkers, E. P. A. M.; Geresdi, A.; Watanabe, K.; Taniguchi, T.; et al. Ballistic

Majorana Nanowire Devices. *Nat. Nanotechnol.* **2018**, *13* (3), 192–197. https://doi.org/10.1038/s41565-017-0032-8.

(48) van Wees, B. J.; van Houten, H.; Beenakker, C. W. J.; Williamson, J. G.; Kouwenhoven, L. P.; van der Marel, D.; Foxon, C. T. Quantized Conductance of Point Contacts in a Two-Dimensional Electron Gas. *Phys. Rev. Lett.* **1988**, *60* (9), 848–850. https://doi.org/10.1103/PhysRevLett.60.848.

(49) Kouwenhoven, L. P.; van Wees, B. J.; Harmans, C. J. P. M.; Williamson, J. G.; van Houten, H.; Beenakker, C. W. J.; Foxon, C. T.; Harris, J. J. Nonlinear Conductance of Quantum Point Contacts. *Phys. Rev. B* **1989**, *39* (11), 8040–8043. https://doi.org/10.1103/PhysRevB.39.8040.

(50) van Wees, B. J.; Kouwenhoven, L. P.; van Houten, H.; Beenakker, C. W. J.; Mooij, J. E.; Foxon, C. T.; Harris, J. J. Quantized Conductance of Magnetoelectric Subbands in Ballistic Point Contacts. *Phys. Rev. B* **1988**, *38* (5), 3625–3627. https://doi.org/10.1103/PhysRevB.38.3625.

(51) Fadaly, E. M. T.; Zhang, H.; Conesa-Boj, S.; Car, D.; Gül, Ö.; Plissard, S. R.; Op het Veld, R. L. M.; Kölling, S.; Kouwenhoven, L. P.; Bakkers, E. P. A. M. Observation of Conductance Quantization in InSb Nanowire Networks. *Nano Lett.* **2017**, *17* (11), 6511–6515. https://doi.org/10.1021/acs.nanolett.7b00797.

(52) Nilsson, H. A.; Caroff, P.; Thelander, C.; Larsson, M.; Wagner, J. B.; Wernersson, L.-E.; Samuelson, L.; Xu, H. Q. Giant, Level-Dependent *g* Factors in InSb Nanowire Quantum Dots. *Nano Lett.* **2009**, *9* (9), 3151–3156. https://doi.org/10.1021/nl901333a.

(53) Vaitiekėnas, S.; Whiticar, A. M.; Deng, M.-T.; Krizek, F.; Sestoft, J. E.; Palmstrøm, C. J.; Marti-Sanchez, S.; Arbiol, J.; Krogstrup, P.; Casparis, L.; et al. Selective-Area-Grown Semiconductor-Superconductor Hybrids: A Basis for Topological Networks. *Phys. Rev. Lett.* **2018**, *121* (14). https://doi.org/10.1103/PhysRevLett.121.147701.

(54) Hansen, A. E.; Kristensen, A.; Pedersen, S.; Sørensen, C. B.; Lindelof, P. E. Mesoscopic Decoherence in Aharonov-Bohm Rings. *Phys. Rev. B* **2001**, *64* (4). https://doi.org/10.1103/PhysRevB.64.045327.

(55) Kurdak, Ç.; Chang, A. M.; Chin, A.; Chang, T. Y. Quantum Interference Effects and Spin-Orbit Interaction in Quasi-One-Dimensional Wires and Rings. *Phys. Rev. B* **1992**, *46* (11), 6846–6856. https://doi.org/10.1103/PhysRevB.46.6846.